Dalton Transactions

ROYAL SOCIETY OF CHEMISTRY

PAPER

View Article Online
View Journal | View Issue

Cite this: *Dalton Trans.*, 2024, **53**, 7044

Crystal structure and properties of perovskite-type rubidium niobate, a high-pressure phase of $RbNbO_3$†

Ayako Yamamoto, *[a] Kimitoshi Murase,[a] Takeru Sato,[a] Kazumasa Sugiyama,[b] Toru Kawamata,[b] Yoshiyuki Inaguma,[c] Jun-ichi Yamaura,[d] Kazuki Shitara,[e] Rie Yokoi[e] and Hiroki Moriwake[e,f]

We synthesized a perovskite-type $RbNbO_3$ at 1173 K and 4 GPa from non-perovskite $RbNbO_3$ and investigated its crystal structure and properties towards ferroelectric material design. Single-crystal X-ray diffraction analysis revealed an orthorhombic cell in the perovskite-type structure (space group *Amm*2, no. 38) with a = 3.9937(2) Å, b = 5.8217(3) Å, and c = 5.8647(2) Å. This non-centrosymmetric space group is the same as the ferroelectric $BaTiO_3$ and $KNbO_3$ but with enhanced distortion. Structural transition from orthorhombic to two successive tetragonal phases (Tetra1 at 493 K, Tetra2 at 573 K) was observed, maintaining the perovskite framework before reverting to the triclinic ambient phase at 693 K, with no structural changes between 4 and 300 K. The first transition is similar to that of $KNbO_3$, whereas the second to Tetra2, marked by c-axis elongation and a significant c_p/a_p ratio jump (from 1.07 to 1.43), is unique. This distortion suggests a transition similar to that of $PbVO_3$, where an octahedron's oxygen separates along the c-axis, forming a pyramid. *Ab initio* calculations simulating negative pressure like thermal expansion predicted this phase transition (c_p/a_p = 1.47 at −1.2 GPa), aligning with experimental findings. Thermal analysis revealed two endothermic peaks, with the second transition entailing a greater enthalpy change and volume alteration. Strong second harmonic generation signals were observed across Ortho, Tetra1, and Tetra2 phases, similar to $BaTiO_3$ and $KNbO_3$. Permittivity increased during the first transition, although the second transition's effects were limited by thermal expansion-induced bulk sample collapse. Perovskite-type $RbNbO_3$ emerges as a promising ferroelectric material.

Received 21st January 2024,
Accepted 21st March 2024

DOI: 10.1039/d4dt00190g

rsc.li/dalton

Introduction

Perovskite-type ferroelectrics, such as $BaTiO_3$, are widely recognized as displacement-type ferroelectrics.[1] These compounds were extensively explored in the 1960s and 1970s, particularly within the soft-phonon mode theory framework.[2] A characteristic feature of these materials is the occurrence of ferroelectric transitions in tandem with crystal tructural transitions. Elements such as Ti(IV) and Nb(V), which possess d^0 electronic configurations, are especially promising for designing new ferroelectric materials.

Alkali metal niobates, $ANbO_3$ (where A = Li, Na, and K), are classic examples of ferroelectrics or anti-ferroelectrics.[1] Their structural stability and distortion types can be explained using the tolerance factor ($t = (r_A + r_O)/\sqrt{2}(r_B + r_O)$) in ABO_3, assuming a perovskite structure. $LiNbO_3$ with t = 0.80 adopts its original $LiNbO_3$-type structure, while $KNbO_3$ with t = 1.05 maintains a perovskite structure. Conversely, $RbNbO_3$ with t = 1.07 deviates from the perovskite structure and forms a pseudo-one-dimensional structure[3] due to the larger Rb ion size.

High-pressure synthesis methods have been instrumental in discovering new functional materials. In ABO_3 compounds, simple and dense structures, such as the $LiNbO_3$ and perovskite types, are stabilized at high pressures based on the ionic radii of A and B. For instance, ferroelectric $LiSbO_3$[4] was stabilized as a $LiNbO_3$-type at 7.7 GPa, and ferroelectric $PbVO_3$[5] as a highly distorted perovskite-type was achieved at 4–6 GPa. The

[a]*Graduate School of Engineering and Science, Shibaura Institute of Technology, 307 Fukasaku, Minuma, Saitama, 337-8570, Japan. E-mail: ayako@shibaura-it.ac.jp*
[b]*Institute for Materials Research, Tohoku University, 2-1 Katahira, Aoba, Sendai, 980, Japan*
[c]*Department of Chemistry, Faculty of Science, Gakushuin University, 1-5-1 Mejiro, Toshima-ku, Tokyo 171-8588, Japan*
[d]*Institute for Solid State Physics, University of Tokyo, Kashiwa, Chiba, 277-8581, Japan*
[e]*Nanostructures Research Laboratory, Japan Fine Ceramics Center, 2-4-1 Mutsuno, Atsuta, Nagoya, 456-8587, Japan*
[f]*International Research Frontiers Initiative (IRFI), MDX Research Center for Element Strategy (MDXES), Tokyo Institute of Technology, SE-6, 4259 Nagatsuta-cho, Midori-ku, Yokohama, Kanagawa, 226-8501 Japan*

†Electronic supplementary information (ESI) available. CCDC 2327355. For ESI and crystallographic data in CIF or other electronic format see DOI: https://doi.org/10.1039/d4dt00190g

high-pressure approach is particularly advantageous for suppressing low vapor-pressure element volatilization, such as Na, K, Rb, Hg, Tl, and Pb, due to the synthesis in a closed cell.

An initial brief report on the high-pressure synthesis of perovskite $RbNbO_3$ dates back to 1972.[6] Over the decades, theoretical calculations have predicted the structural stability and ferroelectric properties of $RbNbO_3$, assuming a perovskite structure.[7] Recently, Fukuda and Yamaura reported on the structural transition of perovskite-type $RbNbO_3$ from the orthorhombic to the tetragonal phase at 493 K and its dielectric properties below 300 K.[8] In our study, we present our detailed findings from independent studies on the crystal structure and phase transitions over a broad temperature range (4–1100 K), along with thermal properties measured using thermogravimetry (TG), differential thermal analysis (DTA), and differential scanning calorimetry (DSC), optical properties measured using second harmonic generation (SHG), and dielectric properties. We also discuss *ab initio* calculations related to phonon dispersion and phase stability. These theoretical calculations explain our experimental results well.

Experimental and theoretical methods

Synthesis and characterization

Ambient pressure phase (APP) $RbNbO_3$ was synthesized from dried Rb_2CO_3 (99.9%, Kojundo Chemical Co.) and Nb_2O_5 (99.99%, Kojundo Chemical Co.) with a *ca.* 5% excess of Rb to maintain stoichiometry. The mixture was sintered in a box furnace at 1073 K in air for 10 hours. The APP was then assembled in a gold cell (3.6 mm in diameter and 6 mm in height) with a heater (carbon tube) and an insulator (boron nitride tube), and the pressure medium (pyrophyllite) all within a glove box to prevent reaction with water. A 180-ton cubic-anvil-type press (Try Eng. Co.) was used for high-pressure synthesis. Polycrystalline samples were treated at 1173 K for 0.5 hours at 4 GPa and as single crystals at 1223 K for 0.2 hours, then cooled to 1173 K for 1 hour at 4 GPa. Both were rapidly quenched to 300 K within several seconds. Characterization was performed using powder XRD (SmartLab, Rigaku) with Cu $K\alpha_1$ radiation, scanning electron microscopy and energy dispersive analysis (SEM-EDX) (JCM-6000 NeoScope, JEOL).

Structure analyses

Single crystal XRD measurements (Mo Kα) were conducted using an XtaLAB Synergy-S diffractometer (Rigaku). Data collection, cell parameter refinement, and data reduction were conducted using the CrysAlis PRO software.[9] The phase structure was identified using SHELXT,[10] and refinement was performed using SHELXL-14.[11] The crystallographic parameters are provided in Table S1.†

Powder XRD (Cu Kα) measurements at 300–1100 K were carried out using a Bragg–Brentano diffractometer equipped with a furnace (Ultima, Rigaku) using a Pt sample holder (also serving as a heater). Measurements at 4–300 K were performed using a Bragg–Brentano diffractometer (SmartLab, Rigaku) with Cu $K\alpha_1$ radiation on a Cu plate connected to a cold head. Lattice parameters were determined using the whole pattern profile fitting method. Diffraction patterns at 373 K (orthorhombic phase), 533 K (tetragonal phase), and 643 K (tetragonal phase) were analyzed using the Rietveld method using the Z-Rietveld software.[12]

Thermochemical and physical properties

TG, DTA, and DSC were conducted using an integrated thermal property measurement system (ThermoPlus, Rigaku) with a nitrogen gas flow for TG-DTA. The enthalpy change determination for phase transitions was calibrated using a tin standard. The SHG measurements, confirming non-centrosymmetric symmetry and evaluating temperature-dependent polarity, were performed using a modified Kurtz NLO system with λ = 1064 nm (YAG laser) in a temperature range of 300–850 K. Details are provided in the referenced materials.[4] The dielectric properties of the sintered sample (a sliced disk, 3 mm in diameter and 1.5 mm in thickness) were measured using a precision inductance, capacitance, and resistance (LCR) meter (4284A; Agilent, Palo Alto, CA) at frequencies of 10, 50, 100, 200 and 500 kHz and 1 MHz in a temperature range of 300–750 K. Gold electrodes were applied to both sides of the sample using a direct-current sputtering method.

Theoretical calculation

All theoretical calculations in this study were performed using the projector augurated wave (PAW)[13] method based on density functional theory (DFT)[14,15] implemented in VASP code.[16,17] All calculations were performed within the generalized gradient approximation parameterized for solids (GGA-PBE_sol).[18] For the PAW potentials, 2s and 2p electrons for O, 4p, 4d, and 5s electrons for Nb, 3s, 3p, and 4s electrons for K, and 4s, 4p, and 5s electrons for Rb were explicitly treated as valence electrons. A plane-wave cut-off energy of 550 eV was used. The convergence of the total energies was less than 0.016 eV f.u.$^{-1}$ compared to the cut-off energy of 1000 eV. Numerical integration was carried out using a 0.25 Å^{-1} k point mesh within Brillouin zones. The energy convergence with respect to the number of k points was better than that of the cut-off energy. The relaxation procedure was terminated when all residual forces on atoms were smaller than 0.01 eV Å^{-1}. Phonon dispersion calculations were performed using the phonopy code[19,20] with a 2 × 2 × 2 supercell.

Results

High-pressure synthesis and characterization

The complex triclinic APP of $RbNbO_3$ was transformed into a denser orthorhombic perovskite-type structure at a high pressure of 4 GPa, as illustrated in Fig. 1(a). The diffraction pattern confirms that $RbNbO_3$ is isomorphic with $KNbO_3$, as shown in Fig. 1(b), exhibiting a $BaTiO_3$-type distortion. The perovskite phase was not obtained below 2 GPa. In the early

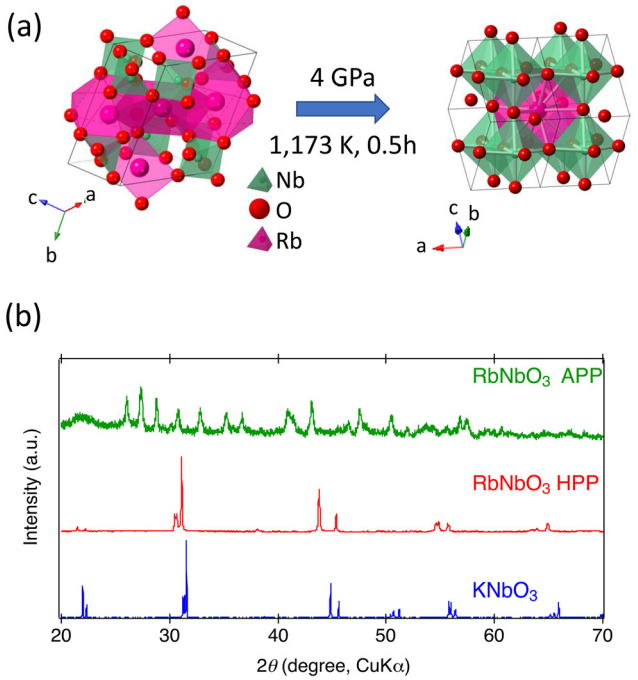

Fig. 1 (a) Crystal structure models of the ambient-pressure phase (APP) and high-pressure phase (HPP) of $RbNbO_3$; (b) powder XRD of APP and HPP of $RbNbO_3$ and $KNbO_3$.

stage of the synthesis, a precursor APP-$RbNbO_3$ was synthesized with slightly off-stoichiometry (Rb deficient), and this induced a small amount of a secondary phase, $Rb_{1-x}NbO_3$ ($x \sim 0.4$) with a tetragonal tungsten bronze (TTB)-type structure. Using a stoichiometric APP-$RbNbO_3$ that began with an Rb-excess composition, $RbNbO_3$ impurity phases were eliminated. Separately from this study, we isolated a single-phase of $Rb_{1-x}NbO_3$ ($x \sim 0.4$) with TTB-type structure, which will be reported elsewhere.

The lattice parameters of $RbNbO_3$ were determined as a = 3.9937(2) Å, b = 5.8217(3) Å, and c = 5.8647(2) Å, and volume v = 136.35(2) Å^3 by single-crystal analysis; consistent with the lattice parameters determined by Fukuda and Yamaura[8] (a = 3.99152(2) Å, b = 5.82230(3) Å, and c = 5.86394(3) Å). These values are larger than those of $KNbO_3$, reflecting the larger ionic size of Rb. The density change from 4.362 g cm^{-3} to 5.514 g cm^{-3} represents a significant volume reduction of 26%, much higher than typical volume reductions in metal complex oxide phase transitions. The orthorhombicity and Nb displacement exceed those of $KNbO_3$, suggesting a higher dielectric polarization.

SEM images in Fig. 2(a–c) show the automorphic grain of HPP-$RbNbO_3$. Most single crystals measured 10–30 μm on the edge length, as shown in Fig. 2(a and b). Most powders and crystals show cubic shapes, but an exception occurs in the case of the Rb-deficient precursor, as seen in Fig. 2(c). The rod-shaped automorphic grain of TTB-$Rb_{1-x}NbO_3$ ($x \sim 0.4$) was confirmed based on both XRD and SEM images. EDX analysis

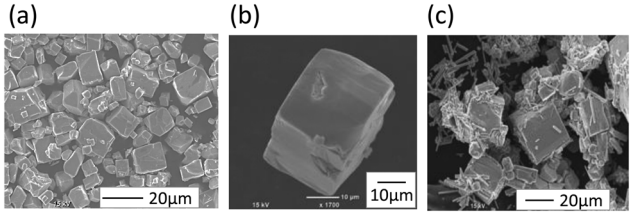

Fig. 2 SEM images of the high-pressure phase of $RbNbO_3$. (a) Granules in bulk, (b) a single crystal, and (c) a sample from a Rb-deficient precursor. Rod-shaped crystals are observed together with cubic crystals (refer to text).

of flat crystal surfaces of $RbNbO_3$ revealed an Rb : Nb ratio of 50.6(4) : 49.4(4), close to the expected stoichiometry.

Atomic positions and displacement parameters in HPP-$RbNbO_3$ were refined using a single-crystal XRD analysis and are listed in Tables 1 and S2.† Bond distances and angles were compared with those of $KNbO_3$ and APP-$RbNbO_3$ and are summarized in Table 2. Fig. 3(a) and (b) illustrate the Nb and Rb coordinations in $RbNbO_3$, respectively. Although cell parameters of $RbNbO_3$ are longer than those of $KNbO_3$, the shortest Nb–O bond is shorter in $RbNbO_3$. The Nb–O bond angles in $RbNbO_3$ deviate more from the ideal 90° than those in $KNbO_3$. A greater Nb shift in the *ab* plane occurring along the polar axis *c* than in $KNbO_3$ was confirmed, resulting in two shorter Nb–O2 bonds and two longer Nb–O2 bonds. The findings suggest a greater polarization in $RbNbO_3$ than that of $KNbO_3$.

The Bond Valence Sum (BVS) calculated[21] for each site, based on the distances in Table 2, indicated that if a cation's BVS exceeds its formal valence, the lattice experiences compression from nearby anions or forms multiple bonds. The BVS value of Rb in HPP-$RbNbO_3$ is exceptionally high at +2.22, indicating significant compressibility with the 12 coordination. In contrast, the BVS for Rb in APP ranged from +0.93–1.20, closer to the formal valence of +1.0. The BVSs of Nb and O1/O2 in HPP are +4.57 and −2.21/−2.29, despite having formal valences +5.0 and −2.0, respectively, suggesting dipole formation.

The *t* was calculated using both Shannon's ionic radii[22] and observed experimental distances. The given *t* for $RbNbO_3$ is slightly larger than for $KNbO_3$. However, once stabilized under

Table 1 Refined crystallographic parameters of the high-pressure phase of $RbNbO_3$ collected using single-crystal XRD at 293 K. The space group is *Amm*2 (no. 38, orthorhombic) with a = 3.9937(2) Å, b = 5.8217(3) Å, and c = 5.8647(2) Å. Detailed information is listed in Table S1.† The U_{ij} is provided in Table S2.† Reliability factors are $R[F^2 > 2\sigma(F^2)]/wR(F^2)$ = 0.0158/0.0366, and S = 1.03

Atom	Site	Occ.	x	y	z	U_{iso} (Å^2)
Nb	2*b*	1	1/2	0	0.50570(9)	0.00383(14)
Rb	2*a*	1	0.0	0	0.02736(6)	0.0062(2)
O1	2*a*	1	0.0	0	0.5487(6)	0.0065(6)
O2	4*e*	1	1/2	0.2411(5)	0.2992(5)	0.0060(4)

Table 2 Selected bond distances, angles, bond valence sum (BVS, ref. 21) values, and tolerance factors (t) of HPP-$RbNbO_3$ and $KNbO_3$ (ICSD#190922), and APP-$RbNbO_3$ (ICSD#16380). t (given) was calculated using Shannon's ionic radii (ref. 22), and t (obs.) was calculated using the experimental distances in the perovskite phase

	$RbNbO_3$ (HPP)	$KNbO_3$	$RbNbO_3$ (APP)
Nb–O2 (Å)	1.854(3) × 2	1.867(2) × 2	Nb1–O, 1.794(5), 1.890(5), 1.948(6), 2.059(4), 2.073(6)
Nb–O1 (Å)	2.013(5) × 2	1.9968(3) × 2	Nb2–O, 1.766(7), 1.912(5),1.996(4), 2.049(5), 2.093(3)
Nb–O2 (Å)	2.288(3) × 2	2.178(2) × 2	—
O1–Nb–O2 (°)	84.60(8)/94.69(7)	85.74(5)/94.58(6)	—
O2–Nb–O2 (°)	89.580(19)	89.67(3)	—
BVS (Rb/K)	+2.22	+1.78	+0.93(Rb1)/+1.20(Rb2)/+1.13(Rb3)
BVS (Nb)	+4.57	+4.63	+4.88(Nb1)/+4.87(Nb2)
BVS (O1)	−2.21	−2.14	−2.03(O1)/−1.28(O2)/−2.12(O3)
BVS (O2)	−2.29	−2.13	−2.28(O4)/−2.15(O5)/−2.40(O6)
t (given)	1.07	1.05	n/a
t (obs.)	1.00	1.00	n/a

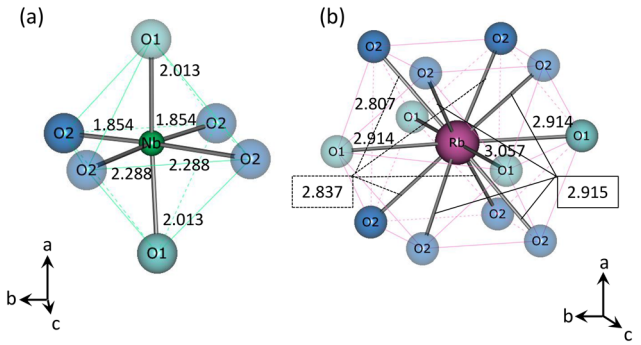

Fig. 3 Structure models of (a) Nb–O and (b) Rb–O coordination in $RbNbO_3$. Numbers between atoms indicates the distance in Å.

high pressure, both the observed t values for the Rb and K variants are 1.00, implying that Rb's ionic radius compacts significantly under high pressure, fitting well within the perovskite structure.

Structural phase transitions depending on temperature

Powder XRD was used to explore temperature-dependent crystal structure changes in $RbNbO_3$ from 300–1100 K. Fig. 4(a) displays the second run's diffraction pattern variation with temperature. At least four phases were identified: an orthorhombic (Ortho) phase, two tetragonal (Tetra1 and Tetra2) phases, and a triclinic phase, as shown in Fig. 4(b). There is likely to be another intermediate phase between Tetra2 and triclinic that is likely a derivative of the triclinic phase. The highest temperature phase reverted to the ambient stable phase above 693 K.

The temperature dependences of the lattice parameters of HPP-$RbNbO_3$ are plotted in Fig. 5. The ortho-to-Tetra1 transition occurred at 493 K, almost the same temperature as in $KNbO_3$.[23] Note that the transition to another tetragonal phase, Tetra2, at 573 K involved lattice parameter c elongation, distinct from the tetra–cubic transition in $KNbO_3$.[23] A wide temperature range with coexisting Tetra1–Tetra2 phases was observed. In this range, c elongated, and the c_p/a_p ratio (a_p and c_p are taken from a basic perovskite cell) increased from 1.07 to 1.43, with cell volume expansion. As later discussed, the SHG was confirmed up to 650 K, proving that the Ortho, Tetra1, and Tetra2 phases are non-centrosymmetric. The space group of both the Tetra1 and Tetra2 phases was estimated as $P4mm$ due to the reflection conditions and appearance of the SHG signal. The Rietveld analyses of powder XRD at 373 K, 533 K, and 643 K were performed, and reasonable parameters are shown in Fig. S2.† Local coordination around Nb in Tetra2 will be discussed later.

Powder XRD measurements at 4–300 K revealed no structural changes, unlike the transition to a rhombohedral phase below 220 K in $KNbO_3$.[24] This aligns with our predictions that the most stable phase, *i.e.*, the lowest energy, of $RbNbO_3$ is the orthorhombic cell, as shown in Table 3, while that of $KNbO_3$ is a rhombohedral cell. The temperature dependences of the diffraction patterns are shown in Fig. S1.† The lattice parameters shrunk according to the regular thermal reduction with decreasing temperature. One possible reason why no phase transition occurred is that Rb substitution functions as chemical pressure. The orthorhombic phase is stable at lower temperatures, as observed in $KNbO_3$ under external (physical) pressure.[25]

Optical and dielectric properties

SHG signals of $RbNbO_3$, along with $KNbO_3$ and $BaTiO_3$, were measured at room temperature to confirm optical polarity. The detection of these signals provides insight into whether the structure possesses non-centrosymmetric symmetry. A distinct peak with a relatively high intensity of 750 (normalized to α-SiO_2) was observed in $RbNbO_3$, as depicted in Fig. 6. This intensity is comparable with that of $KNbO_3$ (I/I_{SiO_2} = 762) and slightly lower than that of $BaTiO_3$ (I/I_{SiO_2} = 1289). Given the structural distortion type common to $RbNbO_3$, $KNbO_3$, and $BaTiO_3$—typical ferroelectrics—$RbNbO_3$ is anticipated to be ferroelectric. However, inverse polarization in the P–E loop remains to be confirmed.

The SHG intensity in relation to temperature was measured using a powdered sample, as shown in Fig. S2.† The intensity *vs.* temperature graph displays kinks around 500 K and 600 K

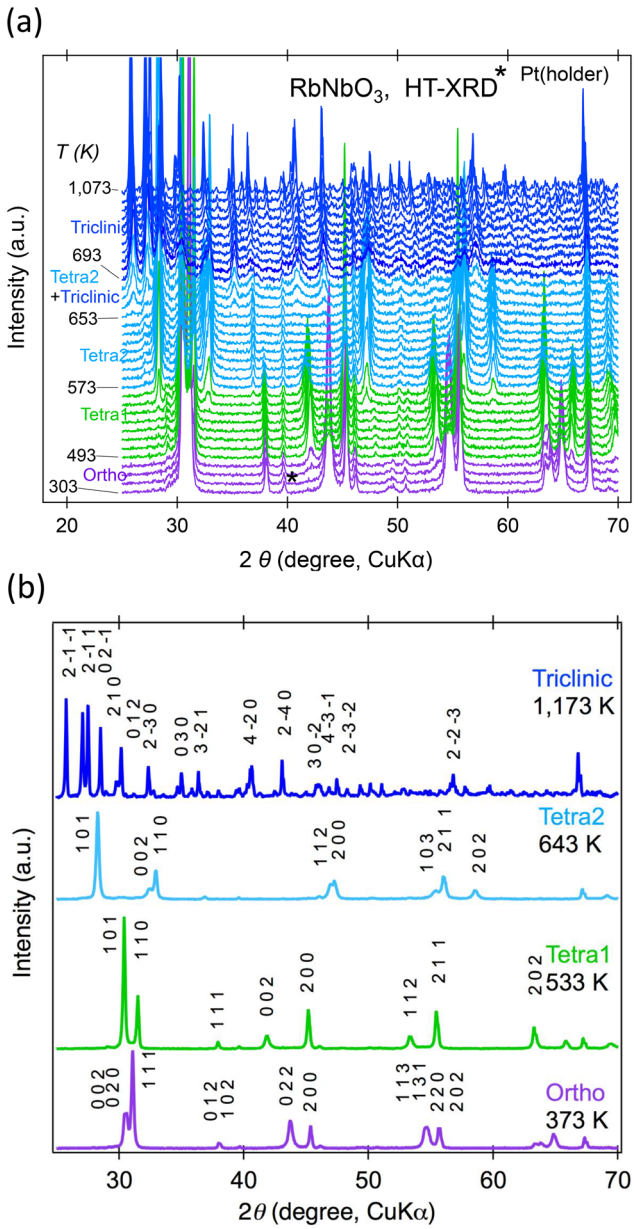

Fig. 4 Temperature dependences of powder XRD patterns for HPP-$RbNbO_3$ at 300–1100 K. (a) Continuous changes in temperatures, and (b) each single phase at selected temperatures. Indexes are indicated only for major peaks.

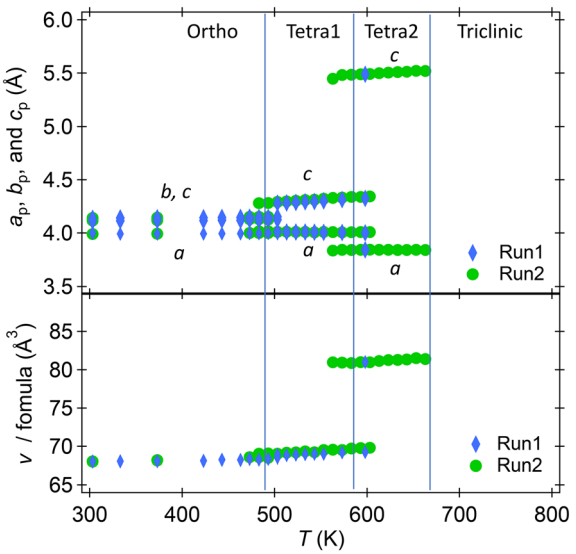

Fig. 5 Temperature dependence of lattice parameters of $RbNbO_3$ at 300–670 K. *a*, *b*, *c*, and *v* taken from a basic perovskite cell.

Table 3 Calculated relative energies of $RbNbO_3$ and related phases based on the energies of the cubic perovskite phase

Space group	$RbNbO_3$ Energy (meV)	$RbNbO_3$ [7] Energy (meV)	$KNbO_3$ Energy (meV)	$BaTiO_3$ Energy (meV)
$Pm\bar{3}m$	0	0	0	0
$P4mm$	−61.76	−46.5	−22.4	−20.4
$Amm2$	−70.11	−57.0	−27.9	−22.5
$R3m$	−70.08	−58.6	−28.9	−27.1

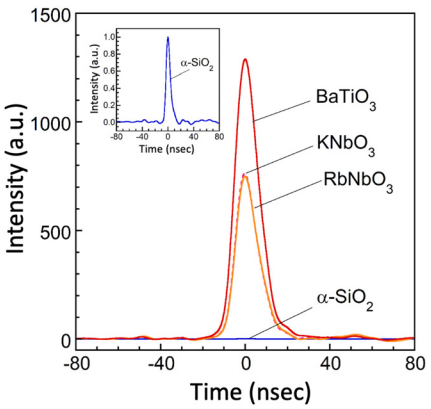

Fig. 6 The second harmonic generation (SHG) signals of perovskite-type $RbNbO_3$, $KNbO_3$ and $BaTiO_3$. The relative intensities were calibrated based on that of α-SiO_2.

in both the heating and cooling processes, with notable hysteresis. The decreasing intensity in the first run might be attributable to domain reformation. These kinks likely correspond to phase transitions from the Ortho to Tetra1 and from the Tetra1 to Tetra2 phases, respectively. This suggests that the Tetra2 structure maintains non-centrosymmetric symmetry similar to the orthorhombic and Tetra1 phases. Further investigation is necessary to clarify the reversibility and hysteresis of these transitions.

The dielectric constant of a disk-shaped bulk of HPP-$RbNbO_3$ with gold electrodes was measured. The permittivity at 350 K was *ca.* 50 (f = 1 MHz), comparable to the value (76 at 200 K, f = 1 MHz) reported by Fukuda *et al.*[8] It gradually increased, showing a sharp rise at the ortho-to-Tetra1 transition temperature, as plotted in Fig. S3.† With further temp-

erature increases, samples collapsed at the Tetra1-to-Tetra2 transition, likely due to significant volumetric expansion. This collapse might be attributable to stress application during measurement, as the samples were fixed with clips. The packing density is about 75% for this measurement. The permittivity at room temperature was 60 at 1 kHz, markedly lower than that of $KNbO_3$. However, we expect the intrinsic value to exceed that of $KNbO_3$, considering the stronger distortion in the Tetra2 phase of $RbNbO_3$ (c_p/a_p = 1.43) compared with the tetragonal phase of $KNbO_3$ (c_p/a_p = 1.04). A bulk sample with higher density or a larger single crystal is required for accurate evaluation. The precise determination of this value is of significant interest for developing high-performance electronic devices.

Thermal analysis

TG and DTA measurements were conducted from 300 K to 1073 K, as shown in Fig. 7(a). Within our instrument's resolution, there were no significant changes in weight in either the heating or cooling cycles. In the DTA, two endothermic peaks and one exothermic peak were observed in the heating process, corresponding to the phase transitions from Ortho to Tetra1 and Tetra1 to Tetra2, and the last for the transition to the triclinic ambient phase. No peaks were found during the cooling process since the transitions did not reverse at ambient pressure once heated to 800 K. To assess the reversibility in the perovskite phase, several phases were quenched from specific temperatures. The orthorhombic phase returns from Tetra1 after being heated at 523 K; however, it does not entirely return from Tetra2. Our quench trial to a pure Tetra2 phase has not succeeded because the phase stability appears to be sensitive to the cooling process at ambient pressure.

Fig. 7(b) illustrates the DSC curves in the heating and cooling processes. The first peak, associated with the ortho–Tetra1 transition above 497 K, showed an enthalpy change (ΔH) of 457 J mol^{-1}, comparable with the O–T transition in $KNbO_3$. In contrast, the second peak above 582 K, corresponding to the Tetra1–Tetra2 transition, indicated a ΔH of 3350 J mol^{-1}, approximately seven times larger than the first transition. This aligns with the observed substantial volume change and is significantly higher than the tetragonal-to-cubic transition in $KNbO_3$,[26] as listed in Table 4. No reversible thermal peaks corresponding to these phase transitions were observed.

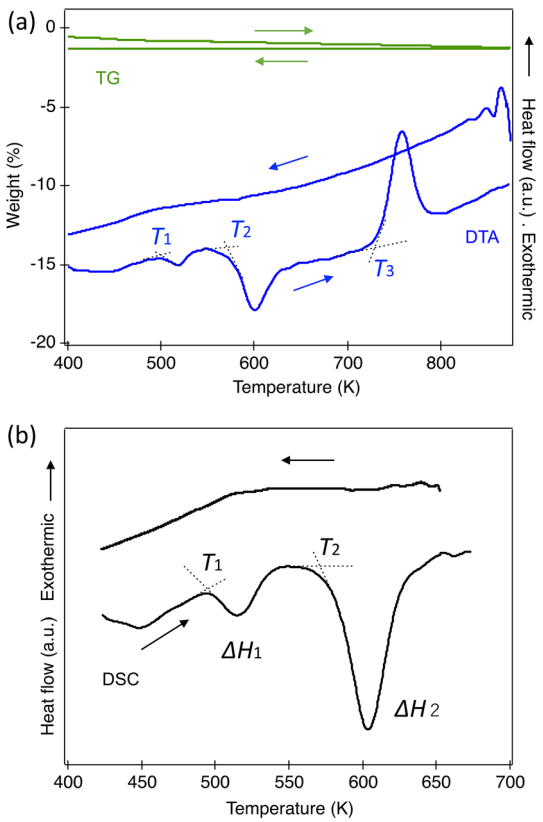

Fig. 7 Thermal analysis of HPP-$RbNbO_3$. (a) TG (left axis) and DTA (right axis), and (b) DSC. In DTA, T_1, T_2, and T_3 are 496 K, 577 K, and 723 K, respectively. In DSC, T_1 and T_2 are 497 K and 582 K, respectively, and the enthalpy changes, ΔH_1 and ΔH_2 with the phase transitions are 457 J mol^{-1} and 3350 J mol^{-1}, respectively. The heating and cooling rates are 20 K min^{-1} in (a) and (b).

Phonon dispersion by *ab initio* calculation

The calculation results for phonon dispersion for virtual cubic perovskite-type $RbNbO_3$ and $KNbO_3$ are shown in Fig. 8. These two compounds showed quite similar phonon dispersion, especially for the soft-mode (imaginary frequency phonon mode). The similar characteristic of the soft-mode phonon around the Γ point, which indicates the potential for displacement-type ferroelectric phase transition, was confirmed. The ferroelectric phase transition of $KNbO_3$ has been confirmed experimentally.[23] Our phonon dispersion calculations suggest the possibility of ferroelectric phase transition in perovskite-type $RbNbO_3$.

Our experimentally obtained orthorhombic perovskite-type $RbNbO_3$ at high pressure was consistent with our first-principles calculations. The calculated relative energies of $RbNbO_3$ depending on symmetries are listed in Table 3. These data indicate the most stable symmetry for $RbNbO_3$ at the lowest temperature is *Amm*2. The energy gap between *P*4*mm* and $Pm\bar{3}m$ is significantly larger than those in $KNbO_3$ and $BaTiO_3$, corroborating that no cubic phase appeared experimentally.

Table 4 Transition temperature and enthalpy of HPP-$RbNbO_3$ and $KNbO_3$[23] determined by DSC

Phase transition	$RbNbO_3$ transition temp. (K)	$RbNbO_3$ enthalpy (J mol^{-1})	$KNbO_3$ transition temp. (K)	$KNbO_3$ enthalpy (J mol^{-1})
Rhomb–Ortho	—	—	260.4	72.47
Ortho–Tetra1	497	457	489	317.71
Tetra1–Tetra2	582	3,350	—	—
Tetra–Cubic	—	—	702	506.89
Tetra2–Triclinic	693 (DTA)	—	—	—

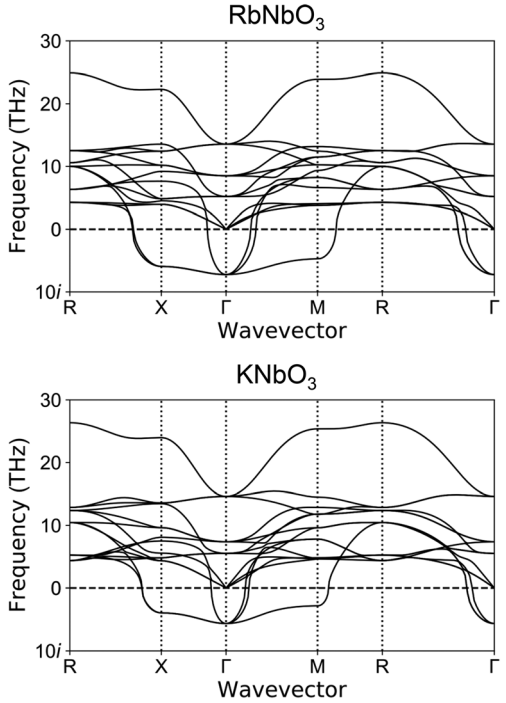

Fig. 8 The phonon dispersions of perovskite-type $RbNbO_3$ and $KNbO_3$.

Discussion

Stabilization of perovskite-type $RbNbO_3$

In $ANbO_3$, where the alkali metal and niobium maintain a 1 : 1 ratio, A = Na and K form perovskite-type structures, while Li, the ion with the smallest radius, forms a $LiNbO_3$-type structure. However, Rb and Cs form unique low symmetry and porous structures because large ions cannot be placed within the perovskite structure. In APP-$RbNbO_3$, Nb–O forms a distorted octahedron 5 + 1 coordination, connecting pseudo one-dimensionally and lacking a three-dimensional network, making it highly hydroscopic and unstable. This study achieved a denser perovskite-type structure in $RbNbO_3$ through a phase transition induced by applying high pressure. The observed 26% volume reduction during this transition is notably large, likely due to the high compressibility of alkali metal ions. It was discovered that the transition to a perovskite phase can occur at 4 GPa, lower than the previously reported 6.5–9 GPa (ref. 6) and 6 GPa (ref. 8) values. Additionally, when reheated under ambient pressure, perovskite HPP reverted to APP above 693 K without decomposition. Our preliminary experiments indicated that the $(Rb_{1-x}K_x)NbO_3$ (x = 0–1) solid solution, isotypic to $RbNbO_3$, can also be achieved at 4 GPa, maintaining the same orthorhombic pristine structure with lattice constants according to Vegard's law.[27]

Of further interest in perovskite $RbNbO_3$ is the feasibility of stabilizing the high-temperature and high-pressure (HTHP) phase as a thin film. $PbVO_3$ [5] was first obtained as an HTHP phase at 4–6 GPa, and then it was obtained as a thin film[28] using the pulsed laser deposition method. As an analogy, we expected that perovskite $RbNbO_3$ could be stabilized as a thin film if we choose substrates with suitable lattice parameters such as $KTaO_3$ (a = 3.989 Å).

Tetragonal to tetragonal phase transition

The first structural phase transition of $RbNbO_3$ from orthorhombic to tetragonal mirrors that of $KNbO_3$.[23] However, the second transition, unlike $KNbO_3$'s transition to cubic, remains tetragonal but with a significant change in axial ratio.

The c_p/a_p ratio increased from 1.07 to 1.43, and the volume expanded by 12%. A similarly strong distortion was reported in tetragonal perovskite $PbVO_3$ (c_p/a_p = 1.22)[5] and $BiCoO_3$ (c_p/a_p = 1.27)[29] that led one tetrahedral oxygen to separate along the c-axis and form a pyramid. Using high-temperature XRD data and Rietveld analysis, as shown in Fig. S4,† we determined the preliminary structural parameters as presented in Table S3.† This transition notably includes one Nb–O bond lengthening from 2.2 Å to 3.0 Å, effectively forming a pyramidal five-coordination as illustrated in Fig. 9.

Such an elongation extent for c has yet to be reported in the $ANbO_3$ series. However, our previous theoretical calculations predicted a tetragonal–tetragonal phase transition by applying negative pressure in an $A'TiO_3$ (A' = Ca, Sr, Ba, and Pb) series. The c_p/a_p ratio of the second tetragonal cell exceeds 1.2, maintaining the space group $P4mm$,[29] which contrasts with the cubic cell with $Pm\bar{3}m$ space group appearing at higher temperatures. For example, in $CaTiO_3$, tetra–tetra phase transition occurs at −4.2 GPa.[29] Inspired by such phase transitions, we calculated the phase stability of HPP-$RbNbO_3$ by applying negative pressure. We found a similar phase transition at −1.2 GPa, as plotted in Fig. 10. The tetragonal phase caused by thermal expansion simulates the lattice expansion under negative pressure. A comparison of experimental lattice parameters and calculated ones assuming negative pressure is provided in Table 5. This suggests the possibility of stabilizing the tetragonal phase with a high c_p/a_p ratio, which is expected to have high permittivity as a thin film by manipulating the lattice size with a suitable substrate.

Dielectric polarization of $RbNbO_3$

In this study, obtaining samples with high packing density was challenging, hindering the estimation of the intrinsic dielectric constant and relative permittivity. Nevertheless,

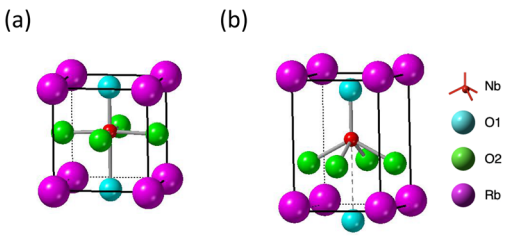

Fig. 9 Structure models of Nb–O coordination in $RbNbO_3$. (a) Tetra1 (c_p/a_p = 1.07), and (b) Tetra2 (c_p/a_p = 1.43) phases.

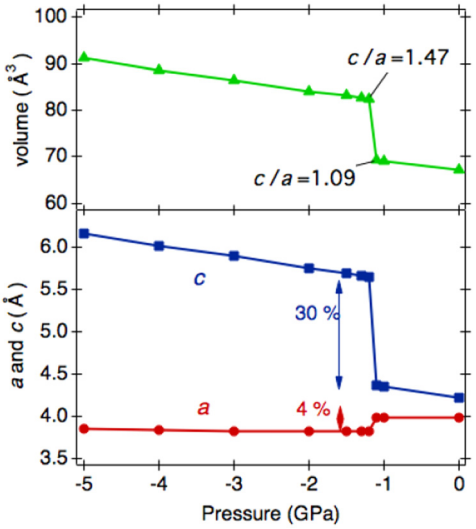

Fig. 10 The calculation of lattice parameters of the tetragonal phase of $RbNbO_3$ assuming negative pressure. Tetragonal–tetragonal transition with an expansion along *c* is predicted by the theoretical calculation.

Table 5 Comparison of experimental lattice parameters by *in-situ* XRD and calculated lattice parameters assuming negative pressure for tetragonal perovskite $RbNbO_3$. XRD patterns from Rietveld analysis are shown in Fig. S4† and refined parameters are listed in Table S3†

Phase, Temp. (K)	Exp. lattice parameters, a (Å), c (Å), and v (Å^3)	Press. (GPa)	Cal. lattice parameters, a (Å), c (Å), and v (Å^3)
Tetra1, 533	a = 4.0080(14) c = 4.3073(15) v = 69.10(2)	0.0	a = 3.992 c = 4.223 v = 69.22
Tetra2, 643	a = 3.8249(12) c = 5.4723(19) v = 80.06(2)	−1.2	a = 3.819 c = 5.650 v = 82.45

given the strong lattice strain, values equal to or greater than those of $KNbO_3$ are anticipated. The dielectric polarization of ortho-$RbNbO_3$, estimated from its Born effective charge,[30] was 0.33 C m^{-2}, closely aligning with $KNbO_3$'s 0.32 C m^{-1}.[31] The dielectric polarizations of the Tetra1 and Tetra2 phases were roughly estimated to be 0.4 and 0.6 C m^{-2}, respectively, comparable with the significant polarization of $LiNbO_3$ and $LiTaO_3$ (0.71 and 0.50 C m^{-2}, respectively).[32] Theoretical calculations under assumed negative pressure also support these findings, maintaining high polarization in Tetra2 even when a bond is broken. Further experiments are planned to measure the dielectric constant and demonstrate high polarization accurately.

Conclusions

We have explored the crystal structures and properties of perovskite-type $RbNbO_3$ synthesized under a high pressure of 4 GPa. The crystal structure, refined at 300 K using single-crystal XRD analysis, was identified as an orthorhombic perovskite (space group *Amm*2, no. 38) with lattice parameters a = 3.9937(2) Å, b = 5.8217(3) Å, and c = 5.8647(2) Å. This structure shares the distortion type seen in $KNbO_3$. Temperature-dependent XRD studies revealed a series of phase transitions: the structure transforms from orthorhombic to tetragonal at 493 K, undergoes another tetragonal transition at 573 K while retaining the perovskite framework, and eventually shifts to the triclinic ambient phase of $RbNbO_3$ at 693 K. Remarkably, no structural changes were observed down to 4 K. The first transition mirrors that of $KNbO_3$, but the second transition presents a unique behavior, notably in the elongation of the *c*-axis and the significant increase in the c_p/a_p ratio from 1.07 to 1.43. Thermal analysis revealed these structural transitions could explain the enthalpy changes. Interestingly, the increase in the lattice parameters in the second transition is an analogy of the theoretical calculation assuming negative pressure. A strong SHG signal, comparable with that of $KNbO_3$, was observed. Further investigation is required to evaluate the permittivity of $RbNbO_3$ accurately and fully understand its potential in ferroelectric applications.

Author contributions

AY: conceptualization, investigation, formal analysis, writing – original draft, and writing – review and editing; KM: data curation and formal analysis; TS: data curation and formal analysis; KS: structural refinement and writing – review and editing; TK: data curation and formal analysis; YI: data curation, formal analysis, and writing – review and editing; JY: data curation and writing – review and editing; KS: theoretical calculation and analysis; RY: theoretical calculation and analysis; HM: investigation, theoretical calculation and analysis, and writing – review and editing.

Conflicts of interest

There are no conflicts to declare.

Acknowledgements

This study was supported by the Kazuchika Okura Memorial Foundation's research grant in 2022–2023 and Innovative Science and Technology Initiative for Security grant number JPJ004596, ATLA, Japan. This study was also supported by the GRIMT program (202212-RDKGE-0018) at the Institute for Materials Research, Tohoku University, and a Joint Research Program (202306-MCBXG-0079) at the Institute of Solid State Physics, University of Tokyo. Powder XRD measurements were performed at Techno-plaza at Shibaura Institute of Technology.

References

1 M. Itoh, Y. Hamasaki, H. Takashima, R. Yokoi, A. Taguchi and H. Moriwake, *Dalton Trans.*, 2022, **51**, 2610–2630.
2 G. Shirane, B. C. Frazer, V. J. Minkiewicz, J. A. Leake and A. Linz, *Phys. Rev. Lett.*, 1967, **19**, 234.
3 M. Serafin and R. Hoppe, *Naturwissenschaften*, 1979, **66**, 50–51.
4 Y. Inaguma, A. Aimi, D. Mori, T. Katsumata, M. Ohtake, M. Nakayama and M. Yonemura, *Inorg. Chem.*, 2018, **57**, 15462–15473.
5 R. V. Shpanchenko, V. V. Chernaya, A. A. Tsirlin, P. S. Chizhov, D. E. Sklovsky, E. V. Antipov, E. P. Khlybov, V. Pomjakushin, A. M. Balagurov, J. E. Medvedeva, E. E. Kaul and C. Geibel, *Chem. Mater.*, 2004, **16**, 3267–3273.
6 J. A. Kafalas, Proc. 5th Mater. Res. Symp. Gaithersburg Md. U. S. Oct. 18–21 1971 NBS Spec Publ No 364 287 1972, 1972, 287–292.
7 A. I. Lebedev, *Phys. Solid State*, 2015, **57**, 331–336.
8 M. Fukuda and K. Yamaura, *J. Ceram. Soc. Jpn.*, 2023, **131**, 126–129.
9 *Rigaku OD*, CrysAlis Rigaku Corp. Oxf. Engl.
10 G. M. Sheldrick, *Acta Crystallogr., Sect. A: Found. Adv.*, 2015, **71**, 3–8.
11 G. M. Sheldrick, *Acta Crystallogr., Sect. C: Struct. Chem.*, 2015, **71**, 3–8.
12 R. Oishi-Tomiyasu, M. Yonemura, T. Morishima, A. Horikawa, S. Torii, T. Ishigaki and T. Kamiyama, *J. Appl. Crystallogr.*, 2012, **45**, 299–308.
13 P. E. Blöchl, *Phys. Rev. B: Condens. Matter Mater. Phys.*, 1994, **50**, 17953.
14 P. Hohenberg and W. Kohn, *Phys. Rev.*, 1964, **136**, B864.
15 W. Kohn and L. J. Sham, *Phys. Rev.*, 1963, **136**, A1133.
16 G. Kresse and J. Furthmüller, *Phys. Rev. B: Condens. Matter Mater. Phys.*, 1996, **54**, 11169.
17 G. Kresse and D. Joubert, *Phys. Rev. B: Condens. Matter Mater. Phys.*, 1999, **59**, 1758.
18 J. Furthmüller, A. Ruzsinszky, G. I. Csonka, O. A. Vydrov, L. A. Constantin, X. Zhou and K. Burke, *Phys. Rev. Lett.*, 2008, **100**, 136406.
19 A. Togo, L. Chaput, T. Tadano and I. Tanaka, *J. Phys.: Condens. Matter*, 2023, **35**, 353001.
20 A. Togo, *J. Phys. Soc. Jpn.*, 2023, **92**, 012001.
21 I. D. Brown, *The Chemical Bond in Inorganic Chemistry: The Bond Valence Model*, Oxford University Press, 2002.
22 R. D. Shannon, *Acta Crystallogr., Sect. A: Cryst. Phys., Diffr., Theor. Gen. Crystallogr.*, 1976, **32**, 751–767.
23 S. L. Skjærvø, K. Høydalsvik, A. B. Blichfeld, M.-A. Einarsrud and T. Grande, *R. Soc. Open Sci.*, 2018, **5**, 180368.
24 G. Shirane, R. Newnham and R. Pepinsky, *Phys. Rev.*, 1954, **96**, 581.
25 Y. Kobayashi, S. Endo, K. Deguchi, L. C. Ming and G. Zou, *Solid State Commun.*, 2001, **120**, 515–517.
26 J. You, G. Li, S. Zhang, X. Zhang, J. Luo, M. Rao and Z. Peng, *J. Alloys Compd.*, 2021, **882**, 160641.
27 A. R. Denton and N. W. Ashcroft, *Phys. Rev. A*, 1991, **43**, 3161.
28 L. W. Martin, Q. Zhan, Y. Suzuki, R. Ramesh, M. Chi, N. Browning, T. Mizoguchi and J. Kreisel, *Appl. Phys. Lett.*, 2007, **90**, 062903.
29 A. A. Belik, S. Iikubo, K. Kodama, N. Igawa, S. Shamoto, S. Niitaka, M. Azuma, Y. Shimakawa, M. Takano, F. Izumi and E. Takayama-Muromachi, *Chem. Mater.*, 2006, **18**, 798–803.
30 X. Gonze and C. Lee, *Phys. Rev. B: Condens. Matter Mater. Phys.*, 1997, **55**, 10355–10368.
31 K. Kakimoto, *J. Crystallogr. Soc. Jpn.*, 2013, **55**, 148–152.
32 M. Minakata, *The Review of Laser Engineering (in Japanese)*, 2004, **32**, 175–180.